CrossMark

Steam Oxidation Behavior of Advanced Steels and Ni-Based Alloys at 800 °C

T. Dudziak, L. Boroń, V. Deodeshmukh, J. Sobczak, N. Sobczak, M. Witkowska, W. Ratuszek, and K. Chruściel

This publication studies the steam oxidation behavior of advanced steels (309S, 310S and HR3C) and Ni-based alloys (Haynes® 230®, alloy 263, alloy 617 and Haynes® 282®) exposed at 800 °C for 2000 h under 1 bar pressure, in a pure water steam system. The results revealed that all exposed materials showed relatively low weight gain, with no spallation of the oxide scale within the 2000 h of exposure. XRD analysis showed that Ni-based alloys developed an oxide scale consisting of four main phases: Cr_2O_3 (alloy 617, Haynes® 282®, alloy 263 and Haynes® 230®), $MnCr_2O_4$ (alloy 617, Haynes® 282® and Haynes® 230®), $NiCr_2O_4$ (alloy 617) and TiO_2 (alloy 263, Haynes® 282®). In contrast, advanced steels showed the development of Cr_2O_3, $MnCr_2O_4$, Mn_7SiO_{12}, $FeMn(SiO_4)$ and SiO_2 phases. The steel with the highest Cr content showed the formation of Fe_3O_4 and the thickest oxide scale.

Keywords	advanced steels, Haynes®, internal oxidation, steam oxidation

1. Introduction

Increased environmental awareness is driving the global economy toward the reduction in CO_2 emissions and fuel consumption. The power energy sector is contributing to these goals by increasing power generation efficiency. It is well known that there is a strong correlation between the temperature and pressure of the steam entering the steam turbine and efficiency of the electrical output (Ref [1-3]). Higher operational temperatures can cause serious problems for boiler components due to their effects on component lifetime, especially when low alloyed steels are used. Steam oxidation of high-temperature-resistant alloys has an important impact on the power plant lifetime and efficiency. Higher operational temperatures significantly accelerate oxidation processes, leading to the development of thick, non-protective Fe-rich oxides with flaky, brittle structures susceptible to scale spallation. Additionally, fast oxide growth and high metal loss significantly reduce heat transfer ability required in order to withstand high steam pressures (Ref [4, 5]). The changes in coal-fired power plants, in respect of temperature and pressure, can be briefly characterized as follows (Ref [6]):

1. 1970s of twentieth century: 538 °C/538 °C/16.7 MPa,
2. 1980s of twentieth century: 540 °C/560 °C/25.0 MPa,
3. 1990s of twentieth century: 560 °C/580 °C/27.0 MPa,
4. Turn of the twentieth and → twenty-first centuries: 600 °C/620 °C/29.0 MPa USC,
5. 2020 of twenty-first century: 700 °C/720 °C/350 MPa A-USC.

As seen, *ultra-super critical* (USC) and *advanced ultra-super critical technology* (A-USC) present the harshest conditions, where the steels developed over 50-60 years ago cannot be used according to the following list (Ref [7]):

1. Ferritic steels: $p < 26$ MPa, 545 °C,
2. Ferritic-Martensitic steels: $p = 26$ MPa, 545 °C,
3. Austenitic steels: 29 MPa, 600 °C,
4. Ni-based alloys: $p > 35$ MPa, $T > 700$ °C.

Even today, steels such as T22 (10CrMo910), T91 (X10CrMoVNb9-10), E1250 (X10CrNiMoMnNbVB15-10-1), 316L (X2CrNiMo18-14-3) and TP347HFG (18Cr9Ni3CuNbN) are broadly used throughout the energy sector; however, those materials do not always meet specifications in the harsh conditions due to the lack of formation of a long-standing Cr_2O_3 thin and stable scale. Currently, particular attention is paid to the materials with a higher Cr content (> 20 wt.%) in order to develop continuous, thin, adherent oxide scales consisting of the Cr_2O_3 phase. Recently, Essuman et al. (Ref [8]) have found that Ni-based alloys rich in Cr develop rich Cr scales; however, the alloys also undergo a deep internal oxidation process. This study was performed on 105, 263 and 740 Ni-based alloys at 800 °C. Two solid solution strengthened alloys: Haynes® 230®, 617 alloy; two (γ') gamma-prime strengthened alloys: 263 and Haynes® 282®; and highly alloyed steels rich in Cr: 309S, 310S and HR3C were tested under 1 bar pressure in a 100% water-steam-water system at 800 °C for 2000 h. The test was carried out in order to compare steam oxidation resistance of the exposed materials, to investigate the phases developed on the exposed surfaces and finally to investigate the internal oxidation penetration depth in relation to Al-Ti ratio.

T. Dudziak, L. Boroń, J. Sobczak, and **N. Sobczak**, Foundry Research Institute, Zakopianska 73, 30-418 Krakow, Poland; **V. Deodeshmukh**, Haynes International, 1020 West Park Avenue, P.O. Box 9013, Kokomo, IN 46904-9013; and **M. Witkowska, W. Ratuszek,** and **K. Chrusciel**, Faculty of Metals Engineering and Industrial Computer Science, AGH University Science and Technology, Al. A. Mickiewicza 30, 30-059 Krakow, Poland. Contact e-mail: tomasz.dudziak@iod.krakow.pl.

2. Experimental Procedure

2.1 Materials

In total, seven materials were exposed: two solid-solution strengthened alloys: alloy 617 and Haynes ®230®; two (γ′) gamma-prime strengthened materials: alloy 263 and Haynes® 282®; and alloyed austenitic steels rich in Cr: 309S, 310S and HR3C. Tables 1 and 2 show compositions according to producer certificates for the Ni-based alloys and high alloyed steels, respectively. The tables show that all the materials in this work possess a high concentration of Cr in order to establish continuous, stable and protective Cr_2O_3 oxide scales.

Prior to the steam test at 800 °C, samples were cut from the plate into small squares [10 × 10 × 2 mm (W × L × T)]. As mentioned, HR3C austenitic steel was delivered as a tube section; the material was machined into a tube segment, with dimensions of ∼15 mm length × 10 mm width and a chord with a 4-mm wall thickness. The surface of the steels and Ni alloys were ground using 600-grit SiC paper. The samples were then cleaned in acetone at 40 °C for 20 min using an ultrasonic bath to remove any grease or other impurities. Samples were weighed before and during exposure using a digital balance with a resolution of $m \pm 0.01$ mg for masses $m \leq 80$ g. Prior to the experiment, samples were weighed three times in order to achieve an accurate measurement. Samples were measured every 250 h in the same manner. Finally, to achieve accurate readings, the balance was calibrated frequently using its internal calibration function and periodic testing with weights.

2.2 Steam Oxidation Experiment

A high-temperature experimental rig, with the ability to produce pure water steam conditions, is presented in Fig. 1. In this type of steam oxidation test setup (Ref 9), 100% pure steam was generated by pumping water from a reservoir placed underneath the furnace. In the furnace, water steam passed over the samples and flowed into a condenser before the water returned to the reservoir. The water used in the reservoir was double deionized. Water was pumped using a peristaltic pump with 1 rpm/min speed, giving 2.830 mL of water/min, (42 L/ 250 h), with a total volume of 330 L after 2000 h of exposure. The whole system was sealed using stainless steel flanges from both ends; prior to the test, the whole system was purged for 2 h using oxygen-free nitrogen (OFN). This purge continues through the water reservoir and throughout the samples exposure period to minimize the level of oxygen in the system in order to reduce the partial pressure of oxygen dissolved from the ambient atmosphere. Prior to exposure, furnace calibration was required in order to detect the hot zone. The samples have been placed on a double-deck plate made of Al_2O_3 in order to avoid any reaction with the plate. The calibration process ensured placement of the samples in the furnace at the test temperature with an accuracy ±5 °C. The heating rate was graduated at a rate of 5 °C/min with the cooling rate after 250 h performed by switching off the mains, cooling the samples down to room temperature with at their natural rate. The peristaltic pump was turned off when temperature in the furnace reached 700 °C in order to avoid condensation of the steam in the furnace.

In this work, kinetic measurements were taken by the traditional discontinuous method, using a digital balance with high accuracy. Post-investigation of the surfaces and cross sections of the exposed samples was performed using macro- and microanalytical techniques. The surface analysis was conducted by using a DSLR Canon EOS 70D camera coupled with a macro lens Canon MP-E 65 mm f/2.8. Microanalysis was carried out using a Hitachi TM3000 tabletop scanning electron microscope (SEM) in backscatter electron mode (BSE). Chemical composition was determined using energy-dispersive x-ray spectroscopy (EDS). Finally, phase development under steam oxidation conditions was examined using the Brag Brentano technique and grazing incidents α = 1° and α = 3°. Metallographic samples for cross-sectional investigations were prepared using conductive resin, PolyFast, supplied by Struers. Further, the samples were ground using 200-μm grinding foil and polished by 9-, 3-, 1- and 0.25-μm diamond suspensions on polishing cloths. The prepared metallographic samples were investigated under the TM3000 SEM in BSE mode.

2.3 XRD Investigations

XRD investigations were conducted using a D500 Kristalloflex with a monochromatic x-ray source, Cu (λKα = 1.54 A) and EMPYREAN PANalytical with a Cu x-ray source using a Ni filter after 1000- and 2000-hour exposures. Phase analysis was performed using two techniques: Bragg-Bentano (BB) geometry and constant angle geometry known as grazing incidence using α = 1° and α = 3°. In Bragg-Bentano (BB) geometry, depth penetration of x-rays can be estimated using the following formula:

$$X = \frac{-\ln(1 - Gx)\sin\theta}{2\mu} \tag{Eq 1}$$

where Gx denotes the intensity of the primary x-ray, giving important information related to the irradiation volume, and μ denotes the linear absorption coefficient
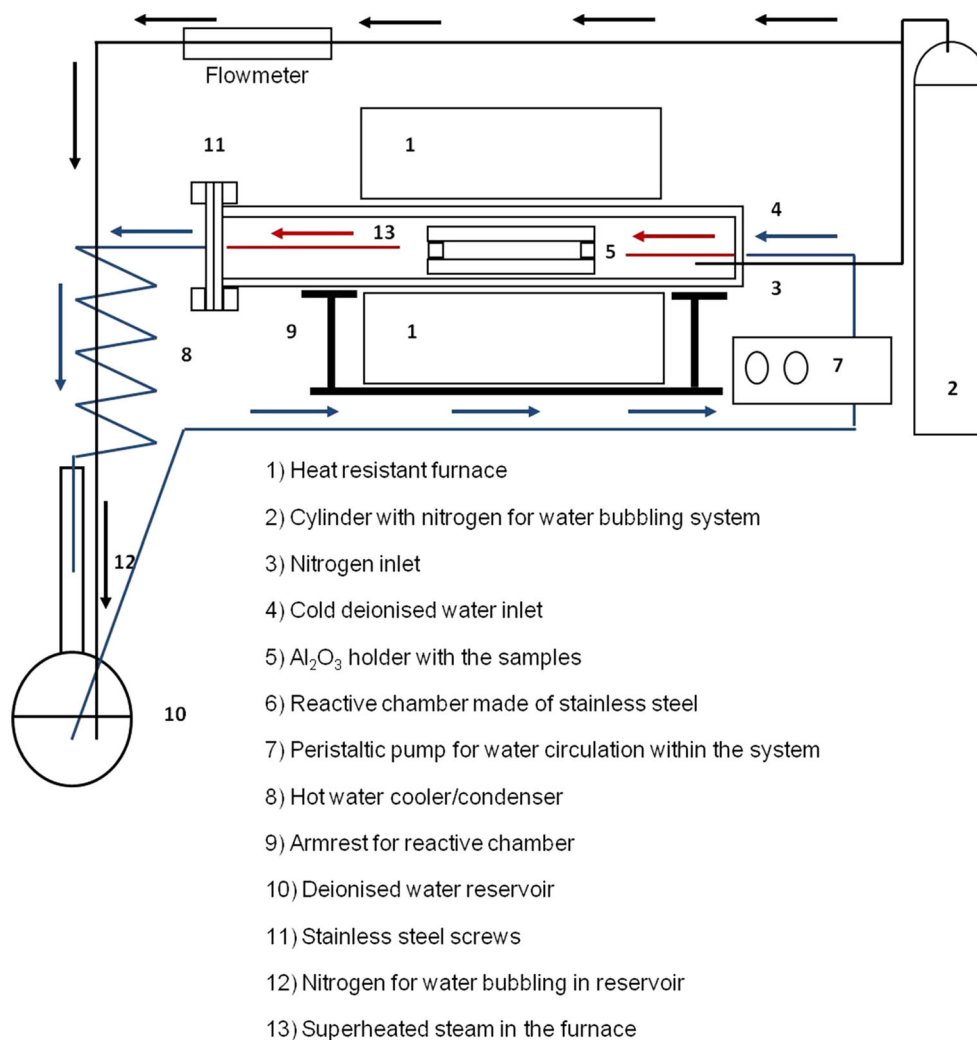
In the grazing angle method, x-rays depth penetration was calculated via the following formula:

Table 1 Chemical composition of Ni-based alloys (wt.%) used in steam oxidation work

	Ni	Fe	Cr	Co	Mo	Si	Mn	Cu	La	Ti	Al	C	W	B
Haynes® 282®	Bal.	1.5	20	10	8.5	0.15	0.3	…	…	2.1	1.5	0.06	…	0.05
Alloy 617	Bal.	1	22	12.5	9	…	…	…	…	0.3	1.2	0.07	…	…
Alloy 263	Bal.	0.6	20	20	6	0.4	0.6	0.2	…	1.2	0.6	0.06	…	…
Haynes® 230®	57	3	22	5	2	0.4	0.5		0.02		0.3	0.1	14	0.015

Table 2 Chemical composition of the highly alloyed steels (wt.%) used in steam oxidation work

	Fe	Cr	Mn	Ni	P	S	Si	C	Nb	N
309S	Bal.	22-24	2	14	0.045	0.03	0.75	0.2		
310S	Bal.	24-26	2	21	0.045	0.03	1.5	0.08		
HR3C	Bal.	25	1.2	20	0.04	0.03	0.4	0.06	0.45	0.2

1) Heat resistant furnace

2) Cylinder with nitrogen for water bubbling system

3) Nitrogen inlet

4) Cold deionised water inlet

5) Al$_2$O$_3$ holder with the samples

6) Reactive chamber made of stainless steel

7) Peristaltic pump for water circulation within the system

8) Hot water cooler/condenser

9) Armrest for reactive chamber

10) Deionised water reservoir

11) Stainless steel screws

12) Nitrogen for water bubbling in reservoir

13) Superheated steam in the furnace

Fig. 1 Steam oxidation rig used in this study

$$X = \frac{-\ln(1 - Gx)}{\left\{ \mu \left[\frac{1}{\sin\alpha} + \frac{1}{\sin(2\theta-\alpha)} \right] \right\}} \quad \text{(Eq 2)}$$

where Gx denotes the intensity of the primary x-ray, giving important information related to irradiated volume, this value is equivalent to 0.95 (95%), μ denotes linear absorption coefficient and α denotes the incidence angle.

The calculated values of Gx, with the assumption of Gx = 95% are listed in Table 3. The results show that penetration depth is dependent on the methodology used; the highest penetration depth was observed when the Bragg-Brentano technique was used with the lowest occurring when the incidence angle $\alpha = 1°$ was used. In general, the x-rays showed a higher penetration depth in the Ni-based alloys than in the advanced steels, and similar findings were found for

grazing incidence measurements: $\alpha = 1°$ and $\alpha = 3°$. The penetration depth corresponds to the incidence angle where a higher angle promotes a higher penetration depth.
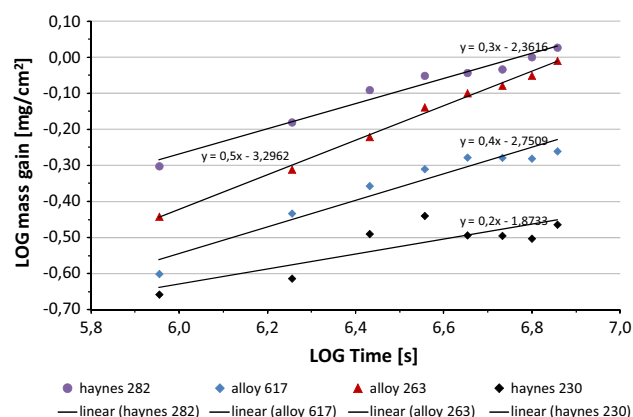
3. Results and Discussion

3.1 Kinetics

Steam oxidation kinetic results at 800 °C for 2000 h for Ni-based alloys and the highly alloyed Fe-based materials with a Cr content higher than 20 wt.% are shown in Fig. 2(a) and (b), respectively. The exposure of highly alloyed steels compared to Ni-based alloys showed slightly better high-temperature corrosion resistance. The steels 309S, 310S and HR3C indicate corrosion resistance between those offered by the alloy 617 and

Table 3 Depth penetration for the oxidized samples at 800 °C for 2000 h

Sample	BB geometry	Grazing incidence α = 1°, μm	Grazing incidence α = 3°, μm
Haynes® 282®	4.64-11.76	0.47	1.35
Alloy 617	4.33-10.96	0.43	1.26
Alloy 263	3.91-9.91	0.39	1.14
Haynes® 230®	4.23-10.71	0.42	1.23
309S	2.58-6.53	0.26	0.75
310S	2.89-7.32	0.29	0.84
HR3C	2.76-6.99	0.28	0.8

(a)

(b)
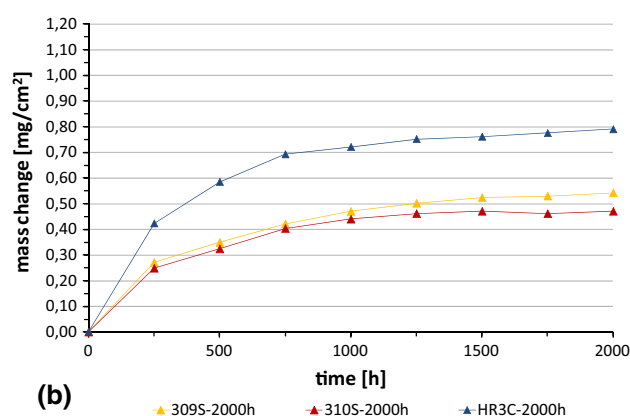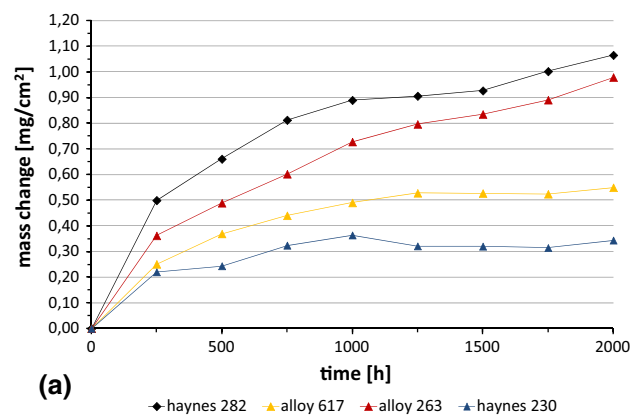
Fig. 2 Mass change data for: (a) Ni-based alloys, (b) highly alloyed steels exposed at 800 °C for 2000 h

Fig. 3 A plot of log mass gain vs. log time to determine the exponent n factor for Ni-based alloys exposed for 2000 h at 800 °C
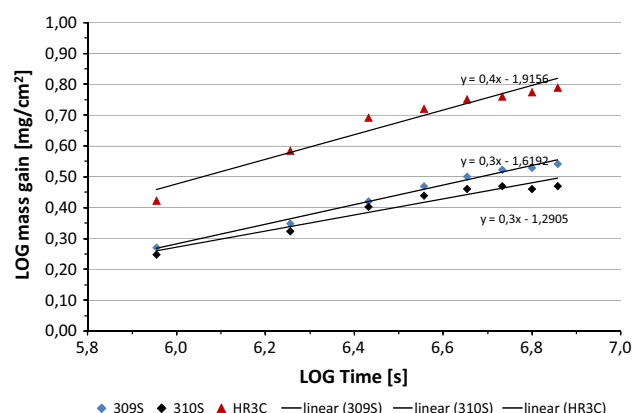
Fig. 4 A plot of log mass gain vs. log time to determine the exponent n factor for advanced steels exposed for 2000 h at 800 °C

the alloy 263, respectively. The poorest corrosion resistance was observed in HR3C, among the exposed austenitic steels. Surprisingly, the lowest corrosion resistance was observed in advanced Ni-based alloy Haynes® 282®. The most promising material, with relatively low mass gain after 2000 h at 800 °C, was Haynes® 230®, and the alloy showed a reduction in mass of approximately 0.9 mg/cm² lower than that offered by Haynes® 282®. Furthermore, it is important to note that heat treatment of Ni-based alloy showed little influence on corrosion resistance. The Haynes® 282® and alloy 263 are (γ′) gamma-prime strengthened alloys, whereas Haynes® 230® and alloy 617 are two solid-solution strengthened alloys, and the results clearly indicate that the (γ′) gamma-prime strengthened alloys showed slightly poorer kinetic behavior, indicating that the oxidation behavior can significantly depend on the phase composition and microstructures of Ni-based or Fe-based substrates. In comparison with Ni-based alloys, two advanced

steels (309S and 310S) containing Si with a concentration more than two and three times higher than that found in HR3C steel, respectively, showed similar behavior in terms of weight change. The alloys 309S and 310S showed almost the same mass gain after 2000 h, whereas the HR3C austenitic steel showed much higher mass despite a much higher Cr content. Nevertheless, some mass loss has been observed between 1500 and 1750 h of exposure at 800 °C in 310S steel.

Figures 3 and 4 show log mass gain vs. log time dependence graphs used for the n-factor calculation for Ni-based alloys and advanced steels, respectively. The figures show that only alloy 263 followed the strict oxidation kinetics related to parabolic law. According to Pieraggi, only a very limited number of

alloys follow the parabolic law, and most of the exposed alloys do not follow these kinetics (Ref 10). The exposed materials, except alloy 263, showed some incoherence in terms of the parabolic mechanism, where values ranging from 0.2 to 0.6 for the n factor have been calculated. The HR3C austenitic steel showed exponent $n = 0.3$ indicating a cubic time dependence law, where the process in most cases can be explained, assuming that oxygen grain boundary diffusion is the domi-

nating scale growth process in combination with an increase in oxide grain size with growth and perhaps with time (Ref 11).

3.2 Macro Observations

The macroobservations shown in Fig. 5(a-g) indicate that the Ni-based alloys and advanced austenitic steels showed high corrosion resistance, where no spallation or cracks in the oxide
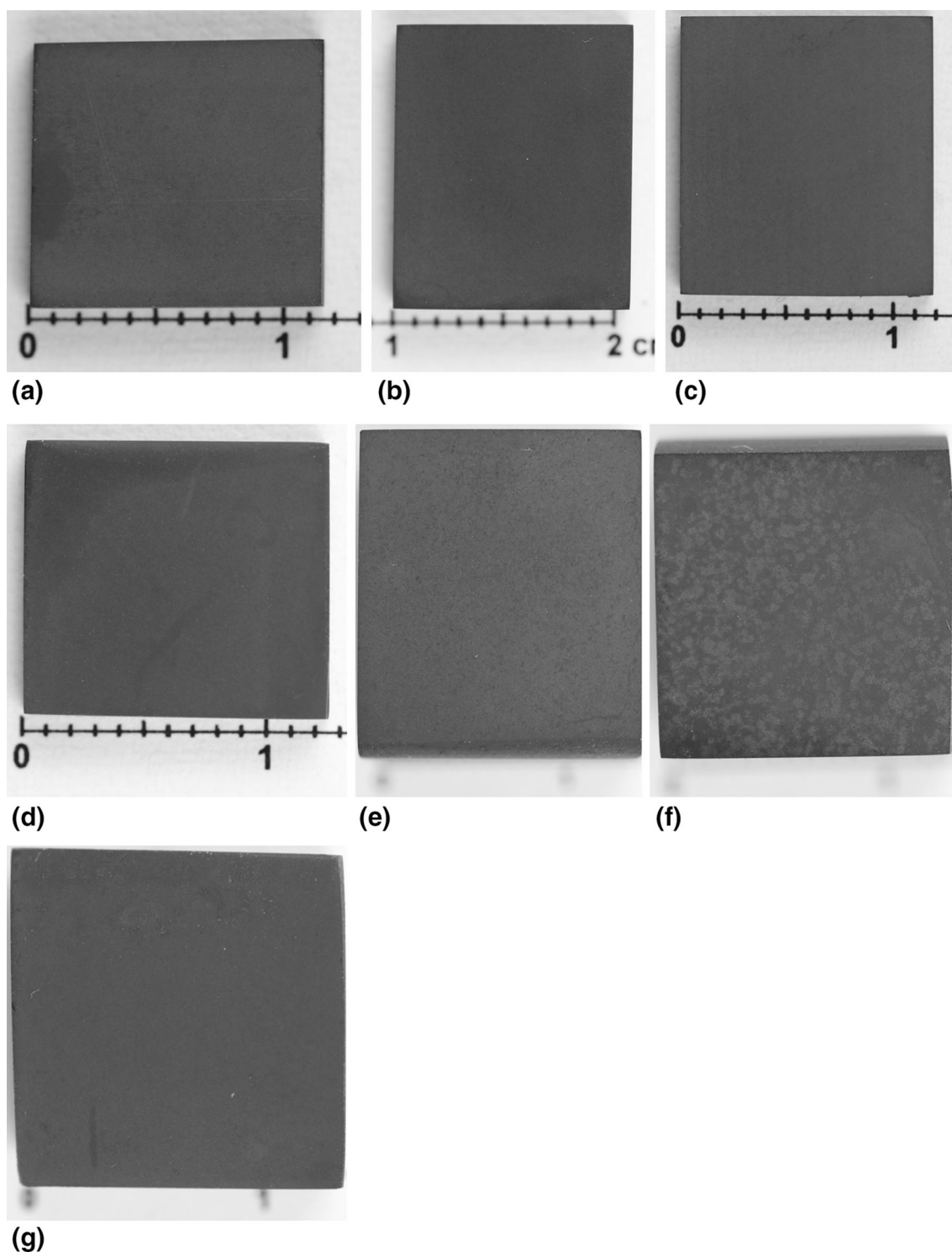
Fig. 5 The oxidized surfaces of the exposed materials in 100% steam conditions for 2000 h at 800 °C: (a) Haynes® 282®, (b) alloy 617, (c) alloy 263, (d) Haynes® 230®, (e) 309S, (f) 310S and (g) HR3C steel

scale were found. Furthermore, the oxide scale developed on the exposed materials showed a high degree of adherence and low surface roughness high smoothness, with no tendency for spallation from the metallic core.

3.3 Surface Microstructures

Figure 6(a-d) shows the surface microstructures of the Ni-based alloys exposed to steam oxidation at 800 °C for 2000 h. The legend presented below the SEM figures in BSE mode shows the concentrations of the main elements found on the exposed surfaces. It should be noted that the exposed surfaces also contained: Co, Ni, Fe, Si; however, these elements were found in low concentrations (below or much lower than 4 wt.%) and are not shown here. The exposed materials showed different microstructures developed under steam oxidation conditions, and the microstructure variations observed are influenced by the processing of Ni-based alloys. Two solid-solution strengthened alloys: alloy 617 and Haynes® 230®, developed the oxide scales richer in Cr in comparison with the two (γ') gamma-prime strengthened alloys: alloy 263 and Haynes® 282®, where oxidation of the Ti from (γ') gamma-prime Ni$_3$(Al,Ti) phase occurred at 800 °C. The observed results are in good correlation with kinetic data, where two (γ') gamma-prime strengthened alloys also indicated a higher mass
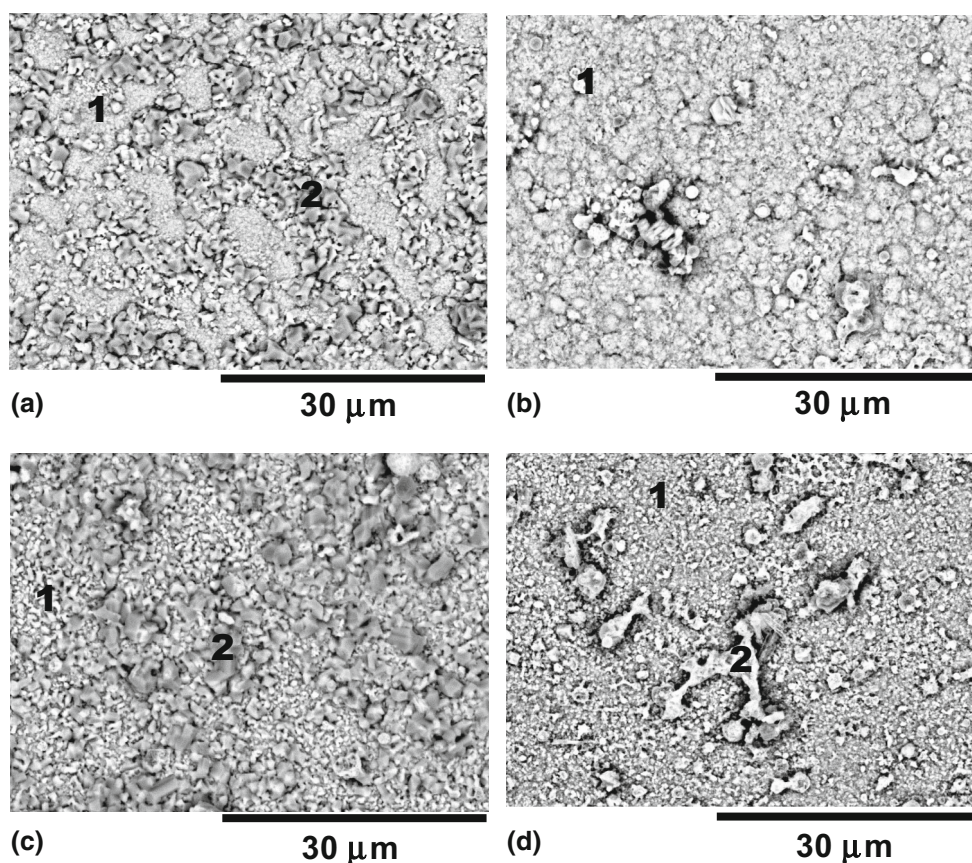
Legend (based on EDS analyses):

Haynes® 282®
1) Cr$_2$O$_3$ + up to 5 wt% Mn and up to 15 wt% Ti
2) TiO$_2$ + 20 wt% Cr
alloy 617
1) Cr$_2$O$_3$ + up to 5 wt% Ni
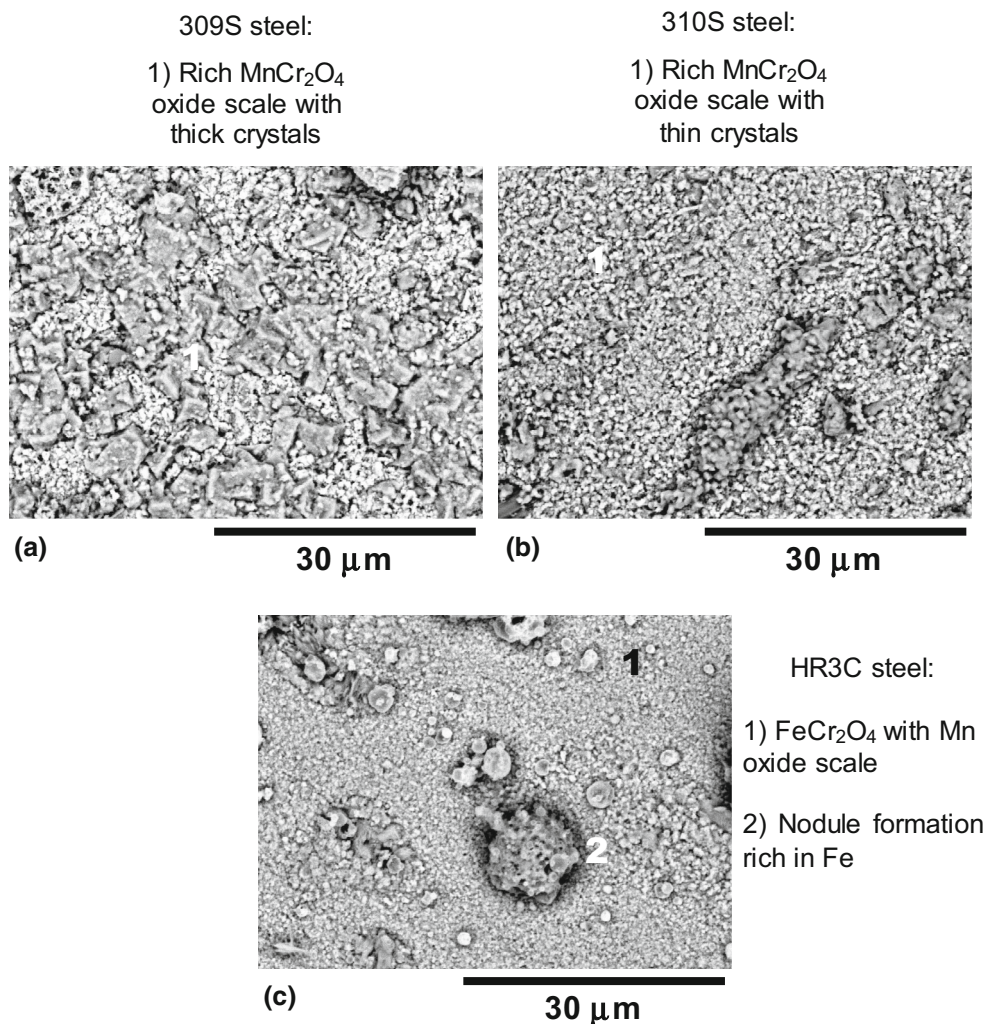alloy 263
1) Cr$_2$O$_3$ + up to 15 wt% Ti
2) TiO$_2$ + 15 wt% Cr
Haynes® 230®
1) Cr$_2$O$_3$ + up to 15 wt% Mn
2) Cr$_2$O$_3$ + up to 25 wt% Mn

Fig. 6 Surface microstructures developed at 800 °C for 2000 h in steam atmosphere for: (a) Haynes® 282®, (b) alloy 617, (c) alloy 263 and (d) Haynes® 230®

309S steel:

1) Rich $MnCr_2O_4$ oxide scale with thick crystals

310S steel:

1) Rich $MnCr_2O_4$ oxide scale with thin crystals

(a) 30 μm   (b) 30 μm

HR3C steel:

1) $FeCr_2O_4$ with Mn oxide scale

2) Nodule formation rich in Fe

(c) 30 μm

Fig. 7 Surface microstructures developed at 800 °C for 2000 h in steam atmosphere for: (a) 309S, (b) 310S and (c) HR3C steel

change than that observed for the two solid-solution strengthened alloys. Furthermore, it has been found that after 2000 h of oxidation Haynes® 230® shows a much better corrosion resistance than that offered by the Haynes® 282® alloy due to a higher concentration of Cr in the metal matrix. In the Haynes® 282®, the Cr reservoir depleted to the critical level, under which TiO_2 crystals started to develop at 800 °C, and this resulted in the formation of a semi-protective scale with tendency to reach higher values of mass change. It is important to note that these two alloys showed higher mass change compared to the Cr-rich steels exposed. Figure 7(a-c) shows the surfaces morphologies of the exposed advanced austenitic steels in a pure steam atmosphere under 1 bar pressure at 800 °C for 2000 h. The surface microstructures developed under steam oxidation conditions vary; however, two advanced austenitic steels with relatively high Si content: the austenitic steels 309S and 310S, showed the development of similar microstructures where mainly Mn, Cr, Si oxides with a low concentration of Fe in the scale were observed. In 309S, the surface was covered by thick crystals with Mn concentrations up to 42 wt.% with thicknesses between 3 and 4 μm. The crystals were evenly distributed on the exposed surface. The surface of 310S austenitic steel, when compared to 309S austenitic steel, developed similar crystals in terms of chemical composition (with 33 wt.% Mn); however, the crystals present were much smaller. Occasionally, the surface microstructure was enriched in Si indicating the formation of Si-containing phases. Under a steam atmosphere, the steel with 25 wt.% Cr developed similarly to 309S and 310S austenitic steels with an adherent, steam oxidation-resistant oxide scale. The crystal structures developed in HR3C austenitic steel showed a different microstructure compared to those observed 309S and 310S steels. Here, the surface microstructure developed in steam conditions at 800 °C formed thinner crystals consisting mainly Fe-Cr elements with the presence of some Mn, suggesting the development of $FeCr_2O_4$ spinel phase with the addition of Mn. In contrast to the 309S and 310S austenitic steels, the Cr-rich austenitic steel, HR3C, developed Fe_3O_4 phase nodules. The nodules have been observed randomly on the surface; the measured size of the nodules reached around 15 μm.

3.4 XRD Studies

XRD analysis of samples was performed after 1000 and 2000 h when the samples were withdrawn from the furnace. Figure 8(a-d) shows XRD patterns for Haynes® 282®, alloy 617, alloy 263 and Haynes® 230®, and Fig. 9(a-c) shows XRD
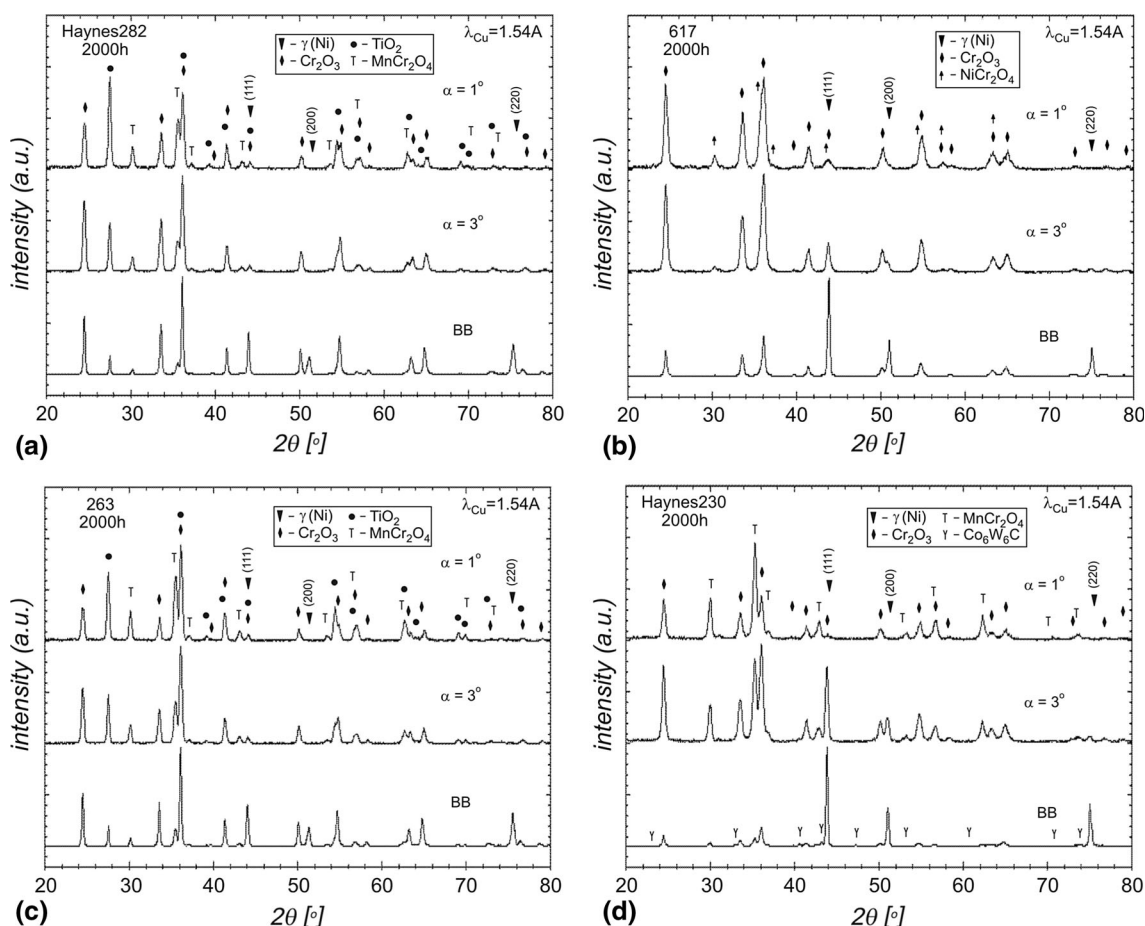
Fig. 8 XRD pattern for (a) Haynes® 282®, (b) alloy 617, (c) alloy 263 and (d) Haynes® 230® exposed at 800 °C for 2000 h in steam conditions

patterns for 309S, 310S and HR3C austenitic steels. It has been found that in the Ni-based alloys the outer layer of the oxide scale has been occupied by Cr_2O_3 and $MnCr_2O_4$ and in the alloy 263 and Haynes® 282®, the formation of the TiO_2 phase as also. The quantity of the TiO_2 phase has been found to be larger after 1000 h than after 2000 h, suggesting decomposition of the phase with time at 800 °C. In the samples investigated after 1000 h, a mostly $MnTiO_3$ phase was observed; however, this phase was not identified after 2000 h (Ref 12). In alloy 617, a $NiCr_2O_4$ was found in addition to $MnCr_2O_4$ and Cr_2O_3. In order to present the XRD results in a clearer way, Table 4 shows the phases developed in the Ni-based alloys under steam oxidation conditions for 2000 h at 800 °C. Similar to the Ni-based alloys, the exposed advanced austenitic steels have been analyzed using XRD. The results revealed that the oxide scales consist mainly of phases related to Cr_2O_3, $MnCr_2O_4$, Mn_7SiO_{12}, $FeMn(SiO_4)$ and SiO_2. Furthermore, it has been observed that a Cr_2O_3 phase has been found in every sample; however, only in the austenitic steel with 25 wt.% of Cr it was found to be the most phase. In the other two austenitic steels, Cr_2O_3 was present, however, as the second most dominating phase (or as a minor part of the oxide scale). As mentioned earlier in this study, the HR3C austenitic steel developed a Fe_3O_4 phase under exposure at 800 °C for 2000 h. The overall phase constituents found under XRD characterization of austenitic steels are listed in Table 5. Results shown in Figs. 8(a-d) and 9(a-c) indicate γ (Ni) phases and γ (Fe)

phases deriving from the metallic core have been observed. Both phases have been blurred with exposure time, indicating oxide scale development. The results correspond to the outcomes listed in Tables 4 and 5, respectively, where in the Ni-based alloys four main phases have been observed: Cr_2O_3 (alloy 617, Haynes® 282®, alloy 263 and Haynes® 230®), $MnCr_2O_4$ (alloy 617, Haynes® 282®, and Haynes® 230®), $NiCr_2O_4$ (alloy 617), and TiO_2 (alloy 263, Haynes® 282®). The exposure of the advanced steels under steam oxidation conditions showed the development of Cr_2O_3, $MnCr_2O_4$, Mn_7SiO_{12}, $FeMn(SiO_4)$ and SiO_2 with some traces of a Fe_3O_4 phase.

3.5 Cross-Sectional Analysis

Figure 10(a-d) shows cross-sectional SEM images in BSE mode of the exposed Ni based at 800 °C for 2000 h. The performed investigations on the cross-sectioned materials revealed that the Ni-based alloys underwent a severe degradation process due to the thick oxide scale formation and a high degree of internal oxidation penetration at 800 °C for 2000 h. The measured thickness of the oxide scale developed under steam oxidation is shown in Fig. 11. The figure reveals that thickness of the oxide scale depends on Cr content in Ni-based alloys; hence, the alloy 617 and Haynes® 230® with 22 wt.% Cr showed the formation of thinner oxide scale than that observed in Haynes® 282® and the alloy 263. The highest
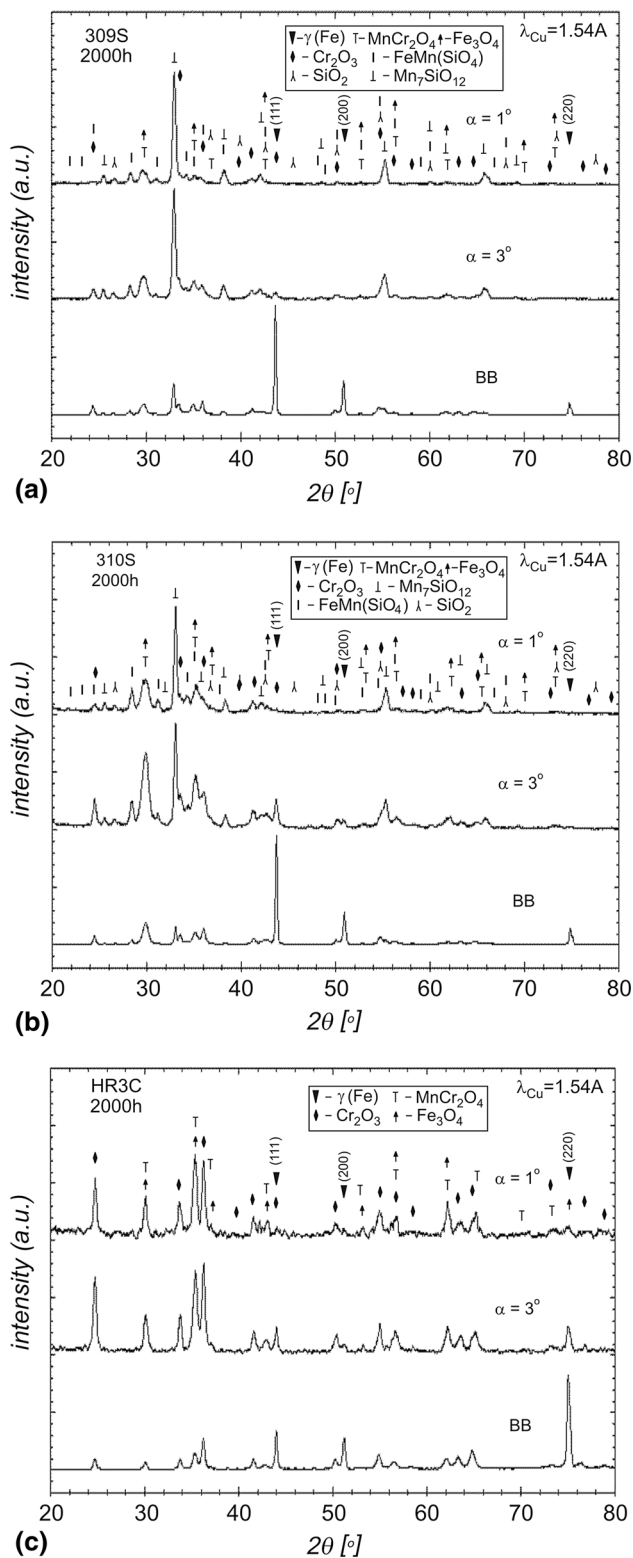
Fig. 9 XRD patterns for (a) 309S, (b) 310S and (c) HR3C exposed for 2000 h at 800 °C in steam conditions

degree of internal oxidation was observed in the two (γ') gamma-prime strengthened alloys: Haynes® 282® and alloy 263 (Fig. 10a, c), and one solid-solution strengthened alloy: alloy 617 (Fig. 10b). For better clarity, Fig. 12 shows the internal oxidation depth vs. Al+Ti concentration [wt.%] in Ni-

based alloys after exposure at 800 °C for 2000 h. It has been found that the highest degree of internal oxidation corresponds to the Haynes® 282® alloy; therefore, it can be suggested that based on the experimental data the presence of Al and Ti in the metal matrix highly enhanced susceptibility to internal oxidation at high temperatures. The process is driven by the ability of Ti and Al to undergo an oxidation reaction due to high negativity of Gibbs free energy formation compared to the other elements in the metal matrix (Si, Ni, Cr, Mn). The formation of TiO_2 and Al_2O_3 require as low as $\Delta G_T^O = -749.6$ and -892.2 KJ mol^{-1} energy to form the oxide. However, the concentration of Al in the Haynes® 282® alloy compared to Ti is much lower resulting in a much more prevalent formation of TiO_2 compared with Al_2O_3. The internal oxidation process is disadvantageous for high-temperature corrosion resistance and has been described many times in the previous studies (Ref 13, 14). Internal oxidation due to the development and precipitation of oxides inside the material is always accompanied by changes in volume through expansion. The volume of expansion generates stresses, which must by some method release. Shida et al. (Ref 15, 16) suggested stress relief mechanisms of grain boundary sliding and extrusion of internal oxide-free metals adjacent to grain boundaries, in the case of intergranular oxidation (Ref 17). It has been observed that mostly Al and Ti have been oxidized internally suggesting the formation Al_2O_3 and TiO_2 phases, respectively (Ref 18). In the Ni-based alloys with some Si content in the metal matrix, SiO_2 formation within the internal oxidation products has also been presented (Ref 14). Thus, corrosion degradation of the Ni-based alloys under steam oxidation conditions can be evaluated in the following way. When clean, the unexposed Ni-based alloys containing 20 or slightly more Cr wt.% are exposed to a steam environment at high temperatures. It is expected that unstable oxides will form under these test conditions. The stability of the phases depends highly on its activity, Gibbs free energy formation, concentration, the partial pressure of the oxidizing gas (pO_2) and finally diffusivity of the elements. At 800 °C, when deionized water is transported from a reservoir to the hot furnace, the following reaction spontaneously occurs:

$$H_2O(l) \rightarrow H_2(g) + \frac{1}{2}O_2(g) \qquad \text{(Eq 3)}$$

$$\Delta G_{H_2O} = 230.000 - 8.14T \cdot \ln(T) + 9.25T \qquad \text{(Eq 4)}$$

Furthermore, when steam surrounds the surface of the exposed alloys immediately, a clean non-oxidized surface of the alloy is covered with the oxidation products. Subsequently, the oxidation of an alloying element and the formation of a particular oxide are determined by, i.e., Gibbs free energy formation, and the values of Gibbs free energy formation can be found elsewhere (Ref 19). Using Gibbs free energy formation and reaction equilibrium equations for the oxides of interest, it is possible to calculate activities for every element. Figure 13 shows log a vs. log pO_2 graph for the elements, and the blue thick stripe indicates log pO_2 in water steam at 800 °C according to work carried out by Dooley (Ref 20). Based on Fig. 13, it has been found that Ti showed the highest activity among the elements, while the Cr, Al and Mn showed the lowest. Nevertheless, a much higher concentration of Cr than Ti in the metal matrix and a relatively negative value of ΔG_T^O for Cr_2O_3 phase at high temperature implies the formation of a

Table 4 Phase constituents in Ni-based alloys exposed in steam conditions; +1 denotes the first most dominating phase, +2 denotes second most dominating phase in the oxide scale, and + denotes presence of the phase detected under XRD analyzer

Sample	Time, h	Geom.	Cr_2O_3	$MnCr_2O_4$	$FeCr_2O_4$	TiO_2	$NiCr_2O_4$	Co_3W_3C
Haynes® 282®	2000	BB	+1	+	+	+2		
		α = 3°	+1	+	+	+2		
		α = 1°	+2	+	+	+1		
Alloy 617	2000	BB	+1				+2	
		α = 3°	+1				+2	
		α = 1°	+1				+2	
Alloy 263	2000	BB	+1	+		+2		
		α = 3°	+1	+		+2		
		α = 1°	+	+2		+1		
Haynes® 230®	2000	BB	+1	+2				+
		α = 3°	+1	+2				
		α = 1°	+2	+1				

Table 5 Phase constituents in the austenitic steels exposed in steam conditions; +1 denotes the first most dominating phase, +2 denotes second most dominating phase in the oxide scale, and +denotes presence of the phase detected under XRD analyzer

| Sample	Time, h	Geom.	Cr_2O_3	$MnCr_2O_4$	$FeMn(SiO_4)$	Mn_7SiO_{12}	SiO_2	Fe_3O_4
309S	2000	BB	+2	+	+	+1	+	+
		α = 3°	+	+2	+	+1	+	+2
		α = 1°	+	+2	+	+1	+	+2
310S	2000	BB	+	+1	+	+2	+	+1
		α = 3°	+	+2	+	+1	+	+2
		α = 1°	+	+2	+	+1	+	+2
HR3C	2000	BB	+1	+2				+2
		α = 3°	+1	+2				+2
		α = 1°	+2	+1				+1

mostly Cr_2O_3-rich oxide scale instead of TiO_2. However, the formation of Cr_2O_3 changed the balance of the elemental activities on the exposed surfaces and oxygen. The development rate of Cr_2O_3 decreases the activity of Cr and the formation of a TiO_2 phase (confirmed by XRD) is observed in the case of alloy 263 and Haynes® 282®. The formation of TiO_2 is favorable instead of Al_2O_3 because activity of Ti at 800 °C is much higher than that presented for Al, despite a slightly more negative ΔG_T^O value for Al_2O_3 formation than for TiO_2. The formation of TiO_2 in Ni-based alloys containing relatively high Ti concentrations shows higher weight gains. It is believed that higher mass gain for γ′ strengthened alloys occurred under steam oxidation conditions due to the development of a TiO_2 phase on the surface. It is well known that the TiO_2 phases possess a high number of defects in the crystal structure and are often responsible for accelerated mass gain in γ-TiAl alloys (Ref 21, 22). Surprisingly, despite the lowest value of activity, the formation of NiO has not been observed, and similar observations have been reported earlier (Ref 4, 14). Under steam oxidation conditions, three Ni-based alloys Haynes® 282®, alloy 263 and Haynes® 230® developed the scale rich in $MnCr_2O_4$, suggesting a high impact of a tiny addition of Mn to the metal matrix. The alloy 617 with no Mn addition to metal matrix at 800 °C developed $NiCr_2O_4$ instead of a $MnCr_2O_4$ spinel. The formation of a $MnCr_2O_4$ spinel

showed beneficial effects for the Haynes® 230® alloy where the lowest weight gain has been found. The improved oxidation performance of the Haynes® 230® alloy among the chromia formers is attributable to the formation of a $MnCr_2O_4$ spinel layer and enhanced further by the presence of a reactive element (0.02 wt.% La) addition (Ref 23). It is believed that the formation of a $MnCr_2O_4$ spinel layer reduces Cr_2O_3 volatilization and the addition of La improves the oxide scale adhesion, thereby improving its oxidation resistance at higher temperatures (Ref 14, 23). Finally, only the alloy 617 showed the formation of $NiCr_2O_4$ as result of diffusion of the Cr^{3+} ions into single-crystal NiO at high temperatures, suggesting the high impact of Mn addition to the γ(Ni) metal matrix. The formation of $NiCr_2O_4$ decreased corrosion resistance in steam conditions in terms of higher weight gain compared that found in Haynes® 230® alloy.

The cross-sectioned microstructures of the austenitic steels are shown in Fig. 14a-c. In contrast to the Ni-based alloys, the advanced austenitic steels indicated the formation of thinner oxide scales as shown in Fig. 15. The findings indicate that the austenitic steel with the highest Cr content developed the thickest oxide scale and the austenitic steel with the lowest Cr content showed the formation of the thinnest oxide scale, and the findings are in contrast to the overall discussion where with increasing Cr content corrosion resistance should be higher, not
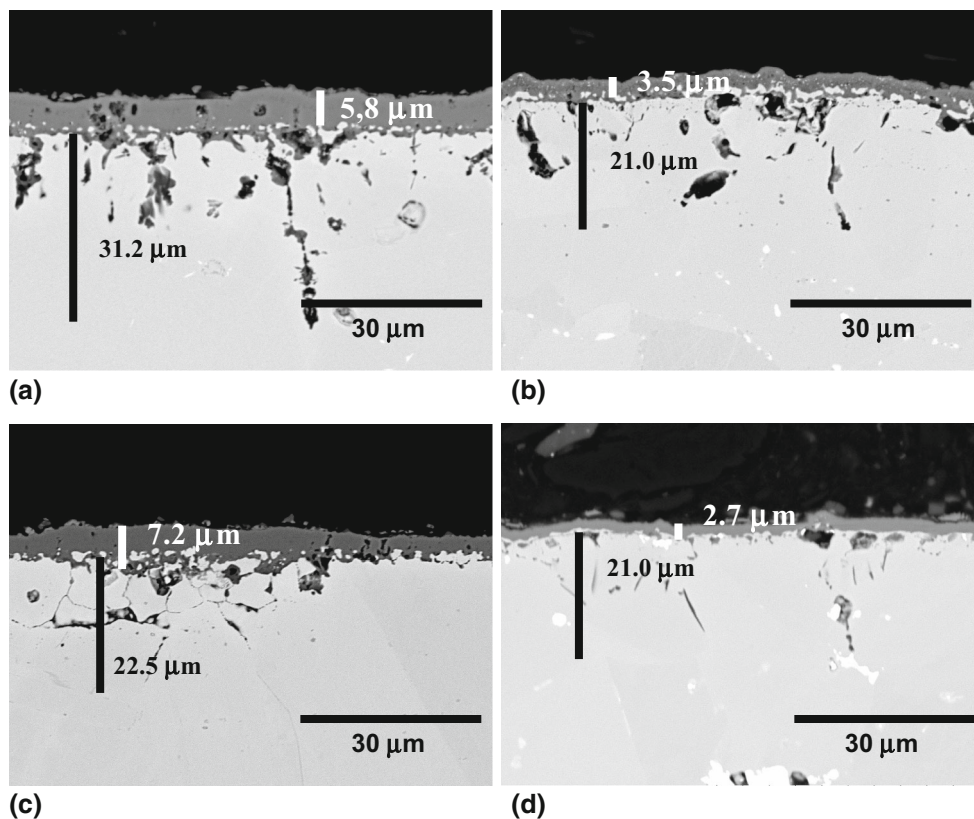
Fig. 10 Cross-sectional microstructures developed at 800 °C for 2000 h in steam atmosphere for: (a) Haynes® 282®, (b) alloy 617, (c) alloy 263 and (d) Haynes® 230®
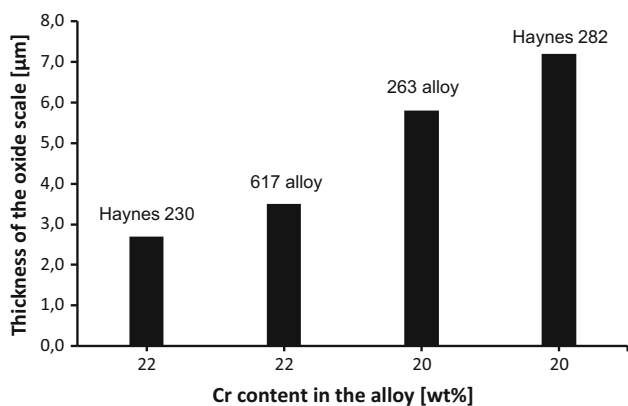
Fig. 11 Thickness of the oxide scale vs. Cr content in the alloy in Ni-based alloys after exposure at 800 °C for 2000 h

Fig. 12 Internal oxidation depth vs. Al+Ti concentration [wt.%] in Ni-based alloys after exposure at 800 °C for 2000 h

lower. The findings can be correlated with another abnormal behavior reported earlier by Ehlers et al. (Ref 24), where in some cases oxidation rates in water-containing environments decrease with temperature, and such a type of behavior is called bell-shaped temperature dependence. Bell-shaped behavior has often been found for steels types T/P91 or VM12.

The austenitic steels, in some areas of the oxide scale, have been covered by randomly distributed crystals. In 309S and 310S, the steels mainly occupied by Mn-rich crystals. In HR3C austenitic steel, nodules have been observed suggesting enrichment of Fe in the oxide scale (Ref 25). The formation of Fe-rich oxide nodules may point to a breakaway mechanism, where transition from a protective oxide scale due to the exclusive
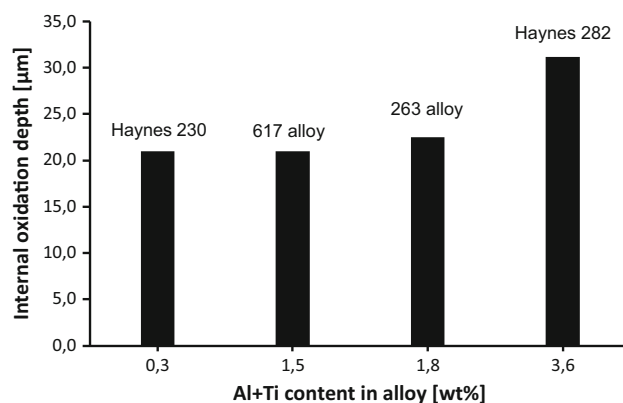
formation of a Cr_2O_3-rich scale transforms into fast oxide growth characterized by the development of iron-rich oxides (Ref 26). Nevertheless, the number of nodules that have been found is relatively low; therefore, the advanced austenitic steels with high Cr content in the metal matrix exposed in this work showed better corrosion resistance than that offered by Ni-based alloys. Better corrosion resistance of the advanced steels resulted from the formation of dense, adherent scales consisting of mainly Cr_2O_3, $MnCr_2O_4$, Mn_7SiO_{12}, $FeMn(SiO_4)$ and SiO_2 phases, with some traces of Fe_3O_4 (309S, 310S), whereas Cr_2O_3, $FeCr_2O_4$ and Fe_3O_4 were observed in HR3C steel.

The steels containing Si in concentrations higher than 0.6 wt.% showed the formation of SiO_2 and other Si-containing

phases, i.e., (Fe, Mn)SiO$_4$. Henry et al. (Ref 27) have shown that addition of Si to the metal matrix of 15 wt.% Cr steels supports breakaway oxidation resistance. In fact, addition of tiny Si quantities to 309S and 310S steels (>20 wt.% Cr) further enhanced the breakaway process, not only because of the high Cr content, high activity and formation of stable Cr$_2$O$_3$, but also due to the effect of Si. The exposed steels, similar to Ni-based alloys, show a lack of evaporation of

Cr from Cr$_2$O$_3$ phase due to the formation of CrO$_2$(OH)$_2$ (g) phase. Lack of an evaporation process is probably due to the formation of a MnCr$_2$O$_4$ spinel under steam oxidation conditions confirmed by XRD. Gordon et al. (Ref 28) reported that Mn additions to steel can reduce the activity of chromium in the oxide, due to the replacement of chromium with manganese from solid solution when low levels of manganese are added, or due to the formation of manganese-chromium spinels when
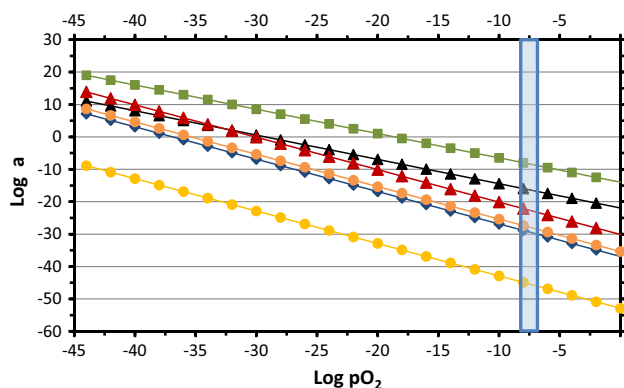
Fig. 13 The minimum activates of Ti, Al, Cr and Ni at 800 °C in steam system
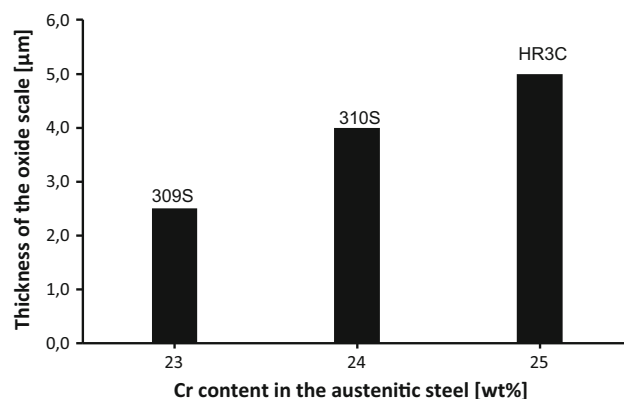
Fig. 15 Thickness of the oxide scale vs. Cr content in the austenitic steels after exposure at 800 °C for 2000 h
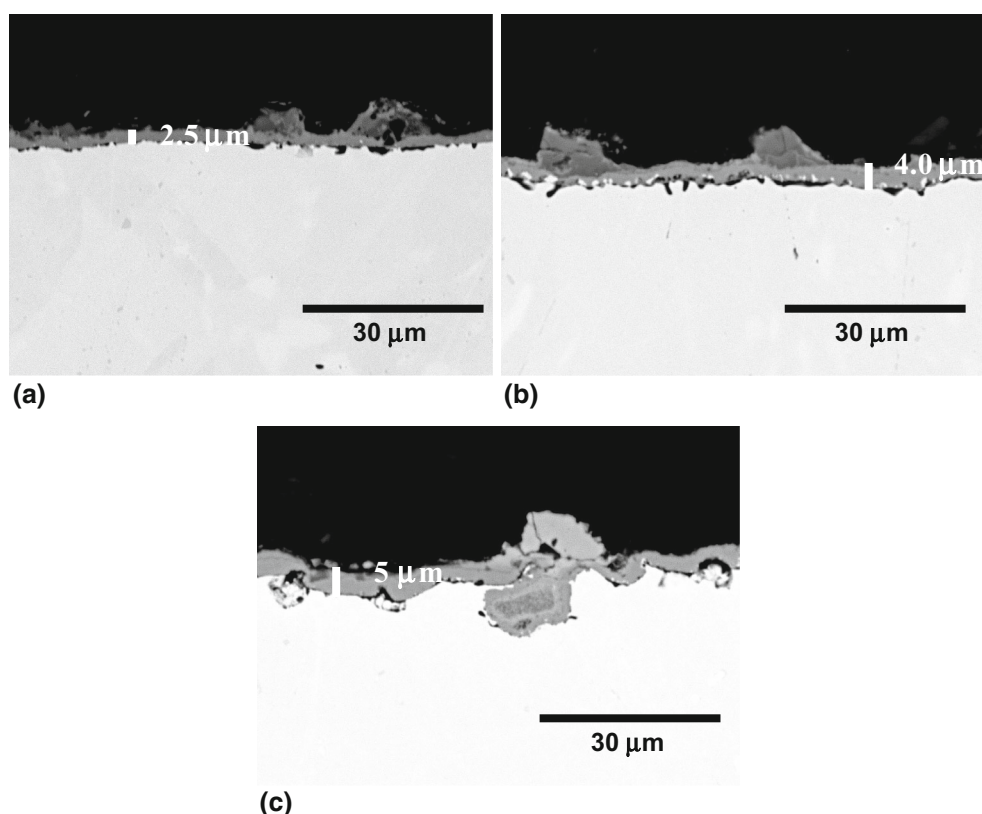
Legend (phases set up based on relevance):

A) 309S: oxide scale: Mn$_7$SiO$_{12}$, Cr$_2$O$_3$, MnCr$_2$O$_4$, Fe$_3$O$_4$ and SiO$_2$
B) 310S: oxide scale: Mn$_7$SiO$_{12}$, MnCr$_2$O$_4$, Cr$_2$O$_3$, Fe$_3$O$_4$
C) HR3C: oxide scale: Cr$_2$O$_3$, MnCr$_2$O$_4$, Fe$_3$O$_4$

Fig. 14 Cross-sectional microstructures developed at 800 °C for 2000 h in steam atmosphere for: (a) 309S, (b) 310S and (c) HR3C steel

high levels of manganese are added. Reduction in chromium activity leads to reduction in chromium evaporation by a factor of 35 at 800 °C. Similarly, the effect of $FeCr_2O_4$ spinel formation may reduce Cr activity and reduce evaporation from the oxide scale containing a rich concentration of Cr, leading to enhancement of corrosion resistance.

4. Conclusions

This paper demonstrates the outcomes of the research performed under steam oxidation of Ni-based alloys and highly alloyed austenitic steels. The study showed that all exposed materials indicated relatively low mass gain after 2000 h at 800 °C, where no cracks, no spallation and no exfoliation of the oxide scale have been found. Furthermore, the study indicates that no chromia evaporation due to the low partial pressure of oxygen under steam conditions has been observed. XRD analysis showed that Ni-based alloys developed mainly Cr_2O_3, $MnCr_2O_4$ oxidation products, the alloy 263 and the Haynes® 282® developed a high quantity of TiO_2. The advanced steels exposed in steam conditions developed mainly Cr_2O_3, $MnCr_2O_4$, Mn_7SiO_{12}, $FeMn(SiO_4)$ and SiO_2 with some traces of Fe_3O_4. The Cr-rich steels showed abnormal behavior in terms of oxide scale thickness, showing thicker oxide scales in the austenitic steel with the highest Cr content.

References

1. N. Komai, F. Masuyama, M. Igarashi, 10-Year Experience with T23 (2.25Cr-1.6W) and T122 (12Cr-0.4Mo-2W) in a Power Boiler, *J Press Vess-T ASME*, 1995, **127** p 190-196
2. J. Gabrel, C. Coussement, L. Verelst, R. Blum, Q. Chen, and C. Testani, Superheater Materials Testing for USC Boilers: Steam Side Oxidation Rate of 9 Advanced Materials in Industrial Conditions, *Mater. Sci. Forum*, 2001, **369–372**, p 931–938
3. W. Quadakkers, P.J. Ennis, J. Zurek, and M. Michalik, Steam Oxidation of Ferritic Steels–laboratory Test Kinetic Data, *Mater. High Temp*, 2005, **22** p 47-60-47
4. I. Wright, A. Sabau, and R. Dooley, Development of Strain in Oxides Grown in Steam Tubes Mater, *Sci. Forum*, 2008, **595–598**, p 387–395
5. I.G. Wright, P.J. Maziasz, F.V. Ellis, T.B. Gibbons, and D.A. Woodford, materials issues for turbines for operations in ultra supercritical steam, *Proceedings of the 29th International Technical Conference on Coal Utilization and Fuel Systems*, 2004, p 1079-1092
6. T.U. Kern, K. Weighthardt, and H. Kirchner, Material and design solutions for advanced steam power plants, *Proceedings of the 4th International Conference on Advances in Materials Technology for Fossil Power Plants. Hilton Head Island, USA*, 2004
7. I. Wright, and R. Dooley, Institute of Materials, Minerals and Mining and ASM International, 2010
8. E. Essuman, L.R. Walker, P.J. Maziasz, and B.A. Pint, Materials Science and Technology, Oxidation Behaviour of Cast Ni-Cr Alloys in Steam at 800 °C, 2013, **29**(7), p 822-827
9. M. Lukaszewicz, N.J. Simms, T. Dudziak, and J.R. Nicholls, Effect of Steam Flow Rate and Sample Orientation on Steam Oxidation of Ferritic and Austenitic Steels at 650 and 700 °C, *Oxid. Met.*, 2013, **79**(5/6), p 473–483
10. B. Pieraggi, Calculations of Parabolic Reaction Rate Constants, *Oxid. Met.*, 1986, **27**(3), p 177–185
11. W.J. Quadakkers, D. Naumenko, E. Wessel, V. Kochubey, and L. Singheiser, Growth Rates of Alumina Scales on Fe-Cr-Al Alloys, *Oxid. Met.*, 2004, **61**(1/2), p 17–38
12. T. Dudziak, V. Deodeshmukh, L. Backert, N. Sobczak, M. Witkowska, W. Ratuszek, K. Chrusciel, A. Zielinski, J. Sobczak, and G. Bruzda, Phase Investigations Under Steam Oxidation Process at 800 & #xB0;C for 1000 h of Advanced Steels and ni-based Alloys, *Oxid. Met.*, 2016, doi:10.1007/s11085-016-9662-8
13. D.J. Young, High temperature oxidation and corrosion of metals, Chapter 6 Alloy Oxidation II: Internal Oxidation, Elsevier 2016
14. V.P. Deodeshmukh, Long-term Performance of High-temperature Foil Alloys in Water Vapor Containing Environment. Part I: Oxidation Behavior, *Oxid Met.*, 2013, **79**(5), p 567–578
15. F.H. Stott, Y. Shida, D.P. Whittle, G.C. Wood, and B.D. Bastow, The Morphological and Structural Development of Internal Oxides in Nickel-aluminium Alloys at High Temperatures, *Oxid. Met.*, 1982, **18**(3/4), p 127–146
16. Y. Shida, F.H. Stott, B.D. Bastow, D.P. Whittle, and G.C. Wood, Development of Preferential Intergranular Oxides in Nickel-aluminium Alloys at High Temperatures, *Oxid. Met.*, 1982, **18**(3/4), p 93–113
17. X. Yu, Z. Jiang, J. Zhao, D. Wie, C. Zhou, and Q. Huang, Effect of a Grain-refined Microalloyed Steel Substrate on the Formation Mechanism of a Tight Oxide Scale, *Corros. Sci.*, 2014, **85**, p 115–125
18. K.A. Christofidou, N.G. Jones, and M.C. Hardy, The Oxidation Behaviour of Alloys Based on the Ni–Co–Al–Ti–Cr System, *Oxid Met.*, 2016, **85**, p 443–458
19. C.B. Alcock, Thermochemical Processes - Principles and Models, Butterworth-Heinemann, ISBN 0 7506 5155 5
20. R.B. Dooley, *Program on technology innovation: Oxide growth and exfoliation on alloys exposed to steam*, Technical Report, Electric Power Research Institute (EPRI) United States, 2007
21. T.S. Bjørheim, A. Kuwabara, and T. Norby, Defect Chemistry of Rutile TiO2 from First Principles Calculations, *J. Phys. Chem. C*, 2013, **117**(11), p 5919
22. H.L. Du, P.K. Datta, Z. Klusek, and J.S. Burnell-Gray, Nanoscale Studies of the Early Stages of Oxidation of a TiAl-base Alloy, *Oxid. Met.*, 2004, **62**(3/4), p 178–193
23. Z.G. Yang, G.G. Xia, J.W Stevenson, P. Singh, Observations on the Oxidation of Mn Modified Ni-Base Haynes 230 Alloy Under SOFC Exposure Conditions U.S. Department of Energy, PNNL-15304 (2005)
24. J. Ehlers, E.J, Smaardijk, A.K, Tyagi, M.Thiele, W.J. Quadakkers, Effect of steel composition on bell shape temperature dependence of oxidation in water vapour containing environments, 14. International Corrosion Congress, 26.9.-1.10.1999, Cape Town, South Africa, Paper No. 336 (1999)
25. P. Tomaszewicz and G.R. Wailwork, Observations of Nodule Growth During the Oxidation of Pure Binary Iron-Aluminum Alloys, *Oxid. Met.*, 1983, **19**(5/6), p 165–185
26. T. Gheno, D. Monceau, and D.J. Young, Kinetics of Breakaway Oxidation of Fe–Cr and Fe–Cr–Ni Alloys in Dry and Wet Carbon Dioxide, *Corros. Sci.*, 2013, **7**, p 246–256
27. S. Henry, A. Galerie, and L. Antoni, Abnormal Oxidation of Stabilized Ferritic Stainless Steels in Water Vapor, *Mater. Sci. Forum*, 2001, **369–372**, p 353–360
28. G.R. Holcomb, D.E. Alman, Department of Energy DOE/ARC-05-002